nature nanotechnology

LETTERS

https://doi.org/10.1038/s41565-018-0323-8

Giant intrinsic photoresponse in pristine graphene

Qiong Ma[1], Chun Hung Lui[2], Justin C. W. Song[3,4], Yuxuan Lin[5], Jian Feng Kong[1], Yuan Cao[1], Thao H. Dinh[1], Nityan L. Nair[1,6], Wenjing Fang[5], Kenji Watanabe[7], Takashi Taniguchi[7], Su-Yang Xu[1], Jing Kong[5], Tomás Palacios[5], Nuh Gedik[1], Nathaniel M. Gabor[2]* and Pablo Jarillo-Herrero[1]*

When the Fermi level is aligned with the Dirac point of graphene, reduced charge screening greatly enhances electron–electron scattering[1–5]. In an optically excited system, the kinematics of electron–electron scattering in Dirac fermions is predicted to give rise to novel optoelectronic phenomena[6–11]. In this paper, we report on the observation of an intrinsic photocurrent in graphene, which occurs in a different parameter regime from all the previously observed photothermoelectric or photovoltaic photocurrents in graphene[12–20]: the photocurrent emerges exclusively at the charge neutrality point, requiring no finite doping. Unlike other photocurrent types that are enhanced near p–n or contact junctions, the photocurrent observed in our work arises near the edges/corners. By systematic data analyses, we show that the phenomenon stems from the unique electron–electron scattering kinematics in charge-neutral graphene. Our results not only highlight the intriguing electron dynamics in the optoelectronic response of Dirac fermions, but also offer a new scheme for photodetection and energy harvesting applications based on intrinsic, charge-neutral Dirac fermions.

Graphene is a model two-dimensional Dirac material with highly tunable transport and optical properties. In particular, it exhibits multiple gate-tunable photocurrent effects, including a thermoelectric photocurrent driven by an electron temperature gradient[14–16,20] and a photovoltaic photocurrent generated by electric fields[12,13,17]. Despite the diversity, all of these photocurrents share a common feature—they are prominent at high charge densities[12–17,20] but are suppressed at the charge neutrality point (CNP). For instance, the thermoelectric photocurrent vanishes at the CNP because the Seebeck coefficient becomes zero when the chemical potential is placed at the Dirac point[14–16,20]; the photovoltaic effect requires strong built-in fields[12,13] or a large external bias[17], which are usually enhanced by (or inevitably involve) a shift of the Fermi level (E_F) from the Dirac point. Therefore, breaking the symmetry of electron–hole occupation by a finite Fermi level usually assists the generation of photocurrents. In this Letter, we uncover a new photocurrent phenomenon in graphene with opposite characteristics—that is. it appears exclusively at the Dirac point and vanishes at high charge densities.

Our observation highlights a unique aspect of interacting Dirac fermions in charge-neutral graphene. Contrary to the conventional scenario where electron–electron scattering facilitates photocarrier relaxation in graphene, the unique electron–electron scattering in charge-neutral graphene can protect the new photocurrent observed in our experiment from being relaxed. Indeed, recent works[6–10,21] have discussed the possibility of highly tunable carrier dynamics in gated graphene. Specifically, it has been predicted that, in the presence of a finite Fermi surface, intraband electron–electron scattering within the linear bands can efficiently relax the photocurrent[10,22,23]. By contrast, when the chemical potential is at the Dirac point, the kinematic constraints of electron–electron scattering across the Dirac point can suppress the photocurrent relaxation[9–11], potentially leading to a robust photocurrent that propagates over a long distance. However, direct experimental evidence of such a novel photocurrent is still lacking. One major challenge is that the high crystalline symmetry of graphene prevents the generation of a net current, whereas near metallic electrodes or p–n junctions (where symmetries are reduced) the signals are usually overwhelmed by conventional thermoelectric and photovoltaic photocurrents.

Here we overcome these difficulties by fabricating graphene devices with special geometrical patterns (see Supplementary Sections 1.1 and 3.4 for further discussions). With such unique device geometries, we observe an anomalous photocurrent that emerges only when the chemical potential is placed at the Dirac point. The photocurrent appears at free graphene edges and is enhanced at edges with sharp bends. The new photocurrent exhibits a distinct gate dependence and spatial pattern from those of conventional photocurrents[12–16,20].

In our experiment, we excite graphene with a focused 850-nm continuous-wave laser and collect the photocurrent through the source and drain electrodes at zero bias[15,20]. Photocurrent images were obtained by scanning the laser spot across the sample (Fig. 1a). All the photocurrent data presented were taken at $T = 90$ K. In the main text, we have chosen four representative devices with different geometries (Figs. 1b,f,j, 2a).

The most distinctive feature of the new photocurrent is its unique gate dependence: it emerges exclusively at the CNP where the Fermi level matches the Dirac point. At high charge densities, we observe conventional photocurrent only near the contacts (Fig. 1c,g,k), as extensively reported in the literature[12–16,20,24]. As we tune graphene to the CNP, the photocurrent at the contacts is suppressed. Instead, a pronounced photocurrent is generated in areas far away from the contacts (Fig. 1d,h,l). Such an anomalous photocurrent at the CNP, with an intensity comparable to that of the contact photocurrent at high density, is hitherto unknown in graphene.

To further investigate the charge density dependence of the anomalous photocurrent, we measured Device 4 with a multiple

[1]Department of Physics, Massachusetts Institute of Technology, Cambridge, MA, USA. [2]Department of Physics and Astronomy, University of California, Riverside, CA, USA. [3]Division of Physics & Applied Physics, School of Physical and Mathematical Sciences, Nanyang Technological University, Singapore, Singapore. [4]Institute of High Performance Computing, Agency for Science, Technology, & Research, Singapore, Singapore. [5]Department of Electrical Engineering and Computer Science, Massachusetts Institute of Technology, Cambridge, MA, USA. [6]Department of Physics, University of California, Berkeley, CA, USA. [7]National Institute for Materials Science, Tsukuba, Japan. *e-mail: nathaniel.gabor@ucr.edu; pjarillo@mit.edu

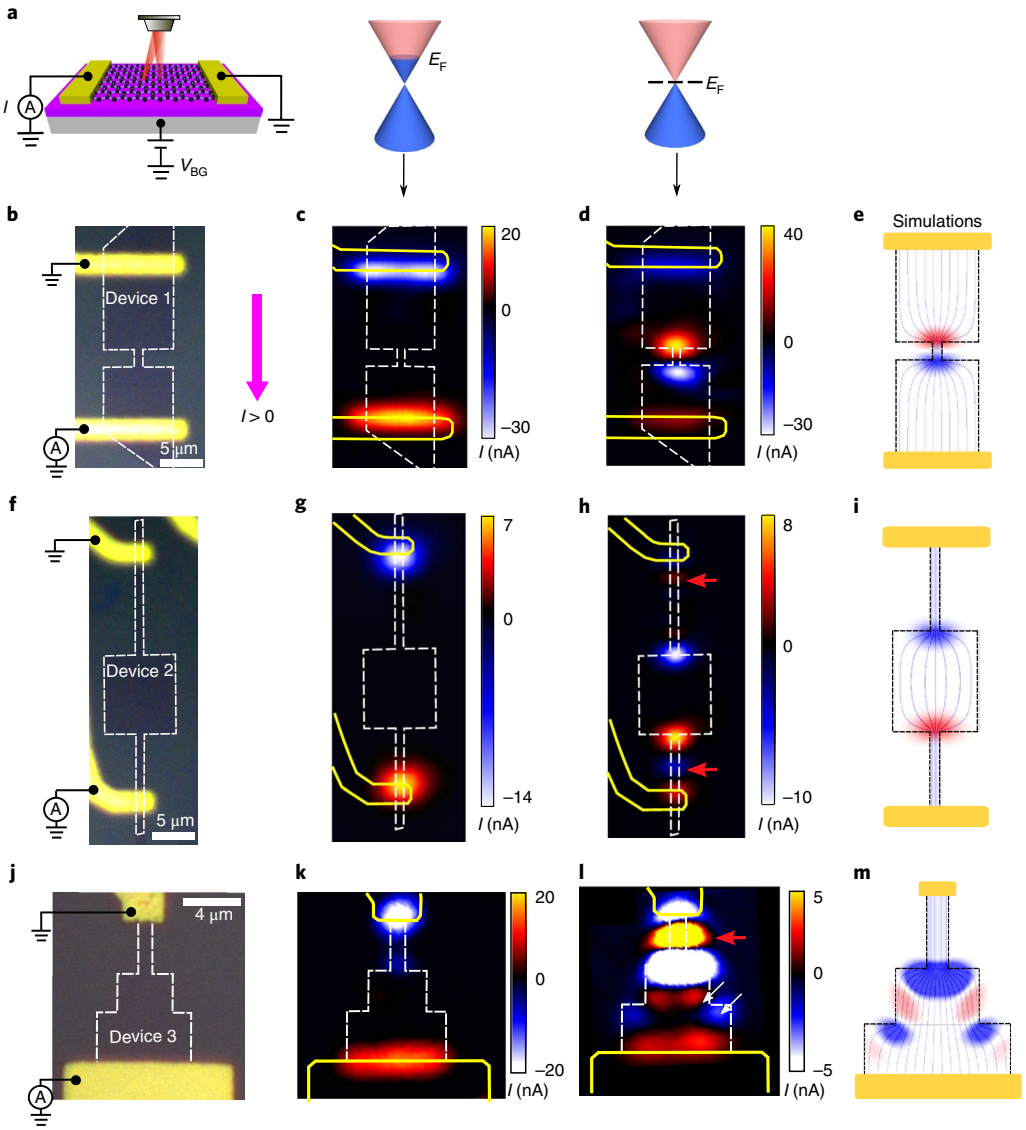

Fig. 1 | Intrinsic long-range edge photocurrent in charge-neutral graphene with different geometries. a, Schematic of a back-gated graphene device with scanning laser excitation. The photocurrent is measured in a short-circuit configuration. **b**–**d**, Optical image (**b**) and scanning photocurrent images (**c**,**d**) of Device 1 with a narrower middle graphene channel. At high charge density (**c**), the photocurrent is mainly generated at the contact areas. At the CNP (**d**), however, significant photocurrent emerges at the two ends of the middle graphene region. **e**, Simulation of the photocurrent image for Device 1. **f**–**i**, Similar figures to **b**–**e**, for Device 2 with a wider middle graphene section. **j**–**m**, Similar figures to **b**–**e**, for Device 3 with three rectangular graphene regions with increasing widths. The white arrows in **l** indicate that the photocurrent is generated from the graphene edge. The red arrows in **h** and **l** denote the photocurrent along the straight edges, which cannot be accounted for by our simple model, but can be captured with some modifications (see Supplementary Information Fig. 28).

cross geometry (Fig. 2). At the CNP, we observe the anomalous photocurrent at all crossings away from the contacts (Fig. 2b). When the chemical potential is tuned away from the Dirac point, the anomalous photocurrent signals vanish abruptly at all the crossings, with nearly the same gating dependence, whereas the contact signal becomes significant at non-zero charge density (Fig. 2d). We notice the following important characteristics by comparing the gate dependences of the photocurrent (Fig. 2f) and the resistance (Fig. 2e): the gate voltage for the anomalous photocurrent peak matches that of the resistance peak; the width of the peak for the photocurrent is narrower than the resistance; and the same feature is found in many other devices with different quality (see Supplementary Section 7). These characteristics further demonstrate that the anomalous photocurrent emerges only at the CNP.

In addition to the unusual density dependence, the anomalous photocurrent has distinct spatial patterns. First, it is prominent at areas with geometric variation, and its magnitude and polarity depend on the local graphene geometry, as clearly shown in the comparative studies of Device 1 and Device 2 (Fig. 1d,h). Second, the photocurrent is generated only from the graphene edges rather than the bulk. In Device 3, with three rectangular graphene regions of increasing widths (Fig. 1j–l), the photocurrent appears at the neck and corner areas (Fig. 1m). As the photocurrent is spatially resolved in the lower (and wider) graphene region, we confirm that only the graphene edges contribute to the photocurrent (white arrows). Such an edge photocurrent is different from the reported photo-Nernst current from graphene edges, which requires the application of a magnetic field[25,26]. Third, the anomalous photocurrent exhibits

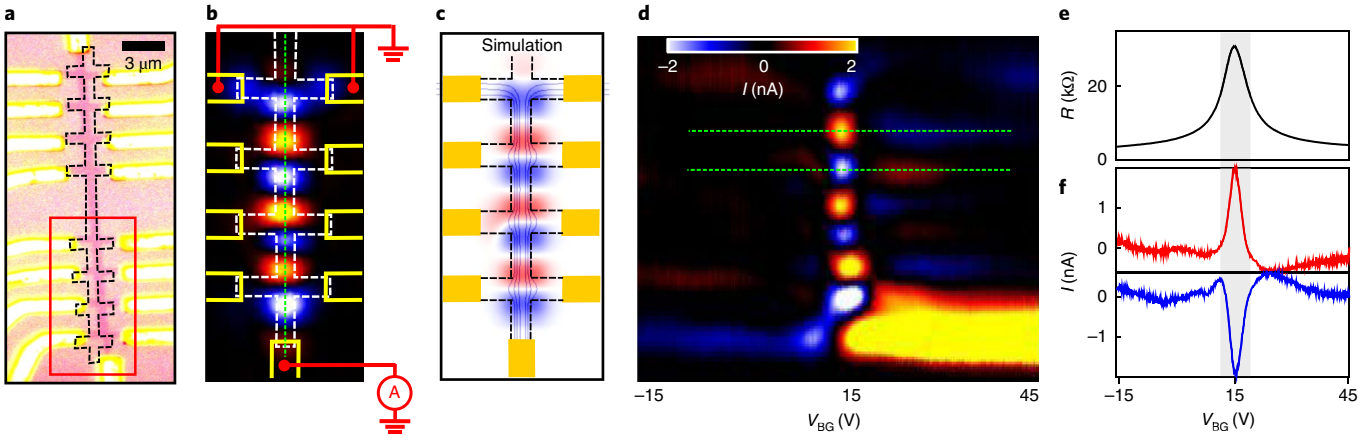

Fig. 2 | Distance and gate dependence of the CNP photocurrent in graphene. a,**b**, Optical image (**a**) and scanning photocurrent image (**b**) of Device 4 with four cross-shaped graphene sections. The four sections have different distances from the collection electrodes located at the upper and lower ends of the device. **c**, Simulation of the photocurrent image of Device 4. **d**, The photocurrent intensity along the vertical middle channel (denoted by the green dashed line in **b**) as a function of gate voltage V_{BG}. **e**, The gate-dependent resistance measured at a small bias voltage of 1 mV. **f**, Representative gate-dependent photocurrents in Device 4, which correspond to the horizontal green dashed lines in **d**. The CNP photocurrent appears only in the shaded region, which is narrower than the resistance peak.

a long-range response. In Device 4, the four cross-shaped graphene sections have the same geometry but different distance from the collection contacts (Fig. 2a,b). We note that such 'long-range' character is not unique to our finding here. Similar 'long-range' phenomena are also found in other systems[13,27,28]. They point to a generic Shockley–Ramo-like photocurrent collection scheme that is important for simulating the photocurrent maps (Supplementary Sections 4.3 and 4.4), as detailed below.

The distinctive gate dependence and spatial patterns of photocurrent hot spots are intriguing. Below we will first analyse the spatial patterns to understand the collection mechanism of the photocurrents, and then further explain the unique gate dependence. The photocurrent collection (an electrically measurable photocurrent signal) requires two steps. First, a local and directional photocurrent ($\mathbf{j}_{local}$) must be generated at the laser excitation spot. Second, this local photocurrent must induce a global current to reach the current-collecting contacts, which are typically micrometres away from the laser excitation area. The location of photocurrent hot spots (edges/corners) strongly suggests that $\mathbf{j}_{local}$ is induced near the edges. Indeed, the generation of $\mathbf{j}_{local}$ is possible only when the spatial circular symmetry is broken. If we photoexcite an area in bulk graphene, the photocurrent flows out radially and cancels out (Fig. 3a). But if we photoexcite the edge, a finite local photocurrent can flow in the perpendicular direction due to the broken reflection symmetry (Fig. 3b). The polarity of $\mathbf{j}_{local}$ is determined by the electron–hole asymmetry present in the system (see Supplementary Section 4.1 for details).

Once a directional $\mathbf{j}_{local}$ is generated at graphene edges, the next question is whether $\mathbf{j}_{local}$ can induce a global current to reach the contacts. As graphene is a conductor, $\mathbf{j}_{local}$ can act as a local electromotive force that drives ambient carriers (see Supplementary Section 4.3 for details). This creates a global diffusion current that flows to the collection electrodes[25,29]. The measured photocurrent, I, can be obtained by the relation $I \propto \int \mathbf{j}_{local}(\mathbf{r}) \cdot \nabla\psi(\mathbf{r})\, d^2\mathbf{r}$ according to the Shockley–Ramo theorem[29], where $\nabla\psi$ is the gradient of the electrical potential (Supplementary Section 4.3). Based on this formula, I is finite only when $\mathbf{j}_{local}(\mathbf{r})$ is not orthogonal to $\nabla\psi$.

To quantitatively understand the observed spatial patterns, we calculate the $\nabla\psi$ field in various device geometries (Supplementary Section 4.3). Figure 3c shows the $\nabla\psi$ field in a device with two different rectangular graphene sections of uniform conductivity. The field lines are approximately parallel to the edges within each section, with nearly zero $\mathbf{j}_{local}(\mathbf{r}) \cdot \nabla\psi(\mathbf{r})$. At the corners, however, the field lines are strongly distorted to give large $\mathbf{j}_{local}(\mathbf{r}) \cdot \nabla\psi(\mathbf{r})$ and hence strong photocurrent (dashed circles in Fig. 3c). Interestingly, with the polarity of $\mathbf{j}_{local}$ fixed, the polarity of the measured photocurrent further depends on the local geometry, as observed in our experiment (Supplementary Section 4). Using this scheme, we have simulated the photocurrent images of Devices 1–4 (Figs. 1e,i,m and 2c) and reproduced all major spatial photocurrent patterns. The excellent agreement further demonstrates that a perpendicular local photocurrent emerges at the graphene edge.

We remark that Devices 2 and 3 also exhibit noticeable photocurrent signals along the straight edges, which cannot be reproduced by our simple model (red arrows in Fig. 1h,l). These additional photocurrent signals can be simulated by assuming a different conductivity at the edge from the bulk, causing bending of field lines even near straight edges, which is a possibility given recent work on edge states in graphene[30–32] (see Supplementary Section 4.3 for further discussion).

Now we turn to explain the unique gate dependence—that is, why the photocurrent is measured only when the chemical potential is placed at the Dirac point. This is related to the nature of the local photocurrent generated near the edges. For a complete analysis, here we consider all the possible photocurrent processes. After the initial optical excitation, the excited electrons will scatter with other degrees of freedom (phonons or other electrons within the Fermi sea, and so on) to reach thermal equilibrium. A photocurrent can be generated before and after thermalization according to different mechanisms. For the photocurrent after thermalization, the photoexcitation raises the graphene temperature, produces a temperature gradient, and induces the photothermoelectric (PTE) current. But the PTE current, being proportional to the Seebeck coefficient, should vanish at the CNP and increase upon electron or hole doping. This is opposite to the gate dependence of our observed CNP photocurrent; we can therefore rule it out (see Supplementary Section 1.1 for further discussions). For photocurrent generation before electron thermalization, a finite (initial) current can be directly realized by optically exciting the electron–hole pairs because electrons and holes have different group velocities at elevated energies. The broken spatial symmetry near the edge allows the formation of a net initial current from the edge (Supplementary Section 4). As we will

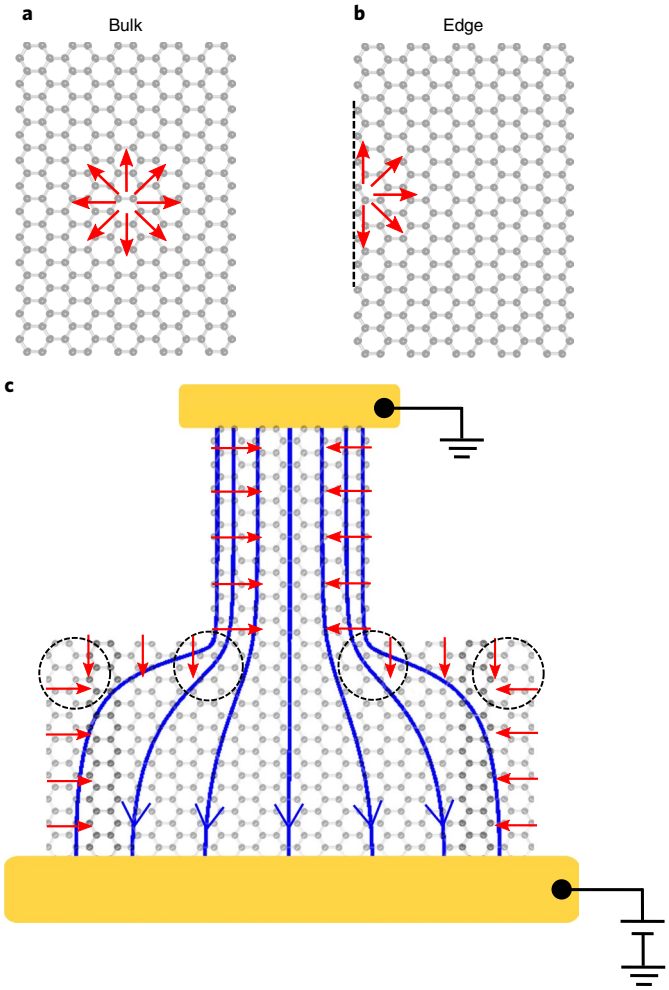

Fig. 3 | Collection of the edge photocurrent in graphene within a Shockley–Ramo-type scheme. a, In the bulk area of graphene, the laser excitation induces an isotropic photocurrent with zero net current (red arrows). **b**, Near the edge with lower symmetry, a finite net photocurrent becomes possible. **c**, Collection of the local photocurrent from the graphene edges in a Shockley–Ramo-type scheme. The blue lines are the weighting field lines of the device with the source at 1 V and the drain at 0 V. The red arrows represent the local edge photocurrent. The dashed circles highlight the regions with strong contributions to the total measured photocurrent.

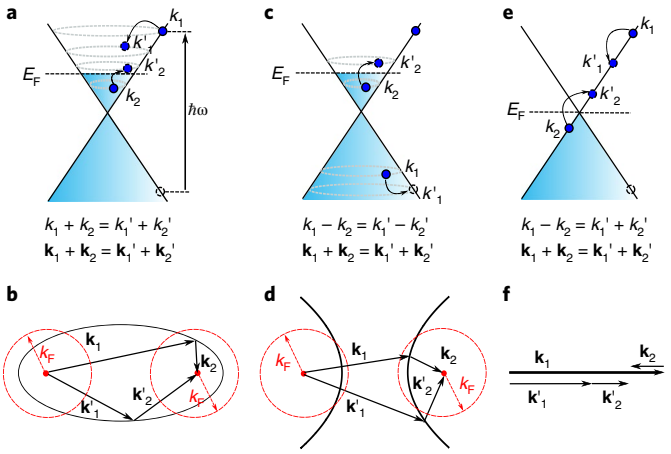

Fig. 4 | Suppression of photocurrent relaxation in charge-neutral graphene. a,**b**, The allowed electron–electron scattering processes for an excited electron in graphene with positive chemical potential (**a**). The conservation of energy and momentum (represented by the equations) constrains the electron wavevectors to an ellipse (**b**). **c**,**d**, Scattering diagram for an excited hole with positive chemical potential (**c**). The electron wavevectors are constrained to a hyperbola (**d**). The situations with negative chemical potential are similar to **a**,**b**. **e**,**f**, Scattering diagram for charge-neutral graphene (**e**). In this case, the electron–electron scattering is limited only to collinear processes, with all four electron wavevectors in the same line (**f**). The total current is preserved after the scattering. In Supplementary Section 6, we provide a detailed derivation for such kinematics, for both perfect linear bands and linear bands with small nonlinear modifications. A related demonstration of the collinear scattering can be found in Lewandowski et al.[11].

show below, the density dependence originates from the relaxation mechanism of the initial current.

The initial current, consisting of highly excited electrons, relaxes through scattering with other particles/excitations in the system. Our systematic analysis (see Supplementary Section 1) shows that scatterings with optical and acoustic phonons, as well as with impurities, relax the initial current. Moreover, these relaxation processes are largely independent of the carrier density. Therefore, they are not responsible for our observed CNP photocurrent, which is sensitive to the charge density. On the other hand, the electron–electron scattering depends strongly on the charge density. As we will elaborate below, electron–electron scattering can suppress the initial current in doped graphene, but not in charge-neutral graphene, due to the unique kinematic constraint in a Dirac system.

To understand the role of electron–electron scattering, we first consider the regime of finite chemical potential, in which intraband processes dominate electron–electron scattering. As an illustration, we consider an excited electron (hole) with initial momentum $\hbar\mathbf{k}_1$ and energy $\hbar v k_1$ and its subsequent scattering with a second electron at $\mathbf{k}_2$ in the Fermi sea. The energy and momentum conservation and Pauli exclusion require:

$$k_1 + k_2 = k_1' + k_2' \tag{1}$$

$$\mathbf{k}_1 + \mathbf{k}_2 = \mathbf{k}_1' + \mathbf{k}_2' \tag{2}$$

$$k_1, k_1', k_2' > k_F > k_2 \tag{3}$$

The left- and right-hand sides of the equations correspond to the states before and after the scattering (Fig. 4a). These relations constrain the final wavevectors ($\mathbf{k}_1'$ and $\mathbf{k}_2'$) in an ellipse set by the initial wavevectors ($\mathbf{k}_1$ and $\mathbf{k}_2$), with differing directions (Fig. 4b). Because the electrons travel at constant speed along the wavevector in the Dirac cone, the total current is not conserved after the scattering. Similarly, the current also changes for an excited hole scattered with an electron within the Fermi sea (Fig. 4c). In this case, the different energy conservation relation $k_1 - k_2 = k_1' - k_2'$ defines a hyperbolic constraint for the final wavevectors (Fig. 4d). In a quantitative calculation[10], the total current of an excited electron–hole pair can be shown to decrease after scattering with other electrons. As the electron–electron scattering time for typical doping levels is extremely short in graphene (<10 fs)[9,18,33], the initial photocurrent is expected to be quenched abruptly.

The initial photocurrent relaxation is, however, very different when the chemical potential is at the Dirac point. In this special case, the intraband processes described above are strongly suppressed due to the vanishing Fermi surface. The only remaining electron–electron scattering process to relax the excited electron (hole) is to produce another electron–hole pair at lower energies (Fig. 4e)[9,10,21].

This interband process requires the momenta of the initial and final states to stay along the same line due to the energy and momentum conservation (Fig. 4f) [9,21]. Such a collinear scattering preserves the total current[10]. In Supplementary Section 6.2, we show that such a conclusion still remains valid when we include a small nonlinear modification to the linear bands. Recent theory indeed predicts a sharp near-collinear angular distribution of secondary carriers in charge-neutral graphene[11]. Therefore, the photocurrent does not decrease after many electron–electron scattering events. The initial local photocurrent can then travel away from the edge and contribute to the global photocurrent (see Supplementary Sections 4 and 5). Because of the suppression of the intraband processes and the unique kinematics of the interband process, this initial local photocurrent $\mathbf{j}_{\mathrm{local}}(\mathbf{r})$ can propagate much further in charge-neutral graphene than in doped graphene. This picture accounts excellently for our observed photocurrent.

In Supplementary Section 3, we present additional, systematic measurements to test the CNP photocurrent's dependence on other parameters, which are summarized as follows: (1) the CNP photocurrent was observed in graphene on different substrates and dielectric environments, including graphene on SiO_2, graphene supported by hexagonal boron nitride (h-BN) and graphene encapsulated by h-BN. (2) The CNP photocurrent was observed in graphene samples with electron mobilities varying from 8,000 to 100,000 $\mathrm{cm^2\,V^{-1}\,s^{-1}}$. (3) The CNP photocurrent was observed by using different laser wavelengths, 600 nm, 850 nm and 10.6 μm. (4) The CNP photocurrent is enhanced as we reduce the density of defects by successive thermal annealings. (5) The CNP photocurrent was observed in all 15 measured devices with either as-exfoliated edges or plasma-etched edges. (6) The CNP photocurrent was observed in the temperature range from $T = 10$ to 300 K. This universality and robustness strongly suggest that the new photocurrent arises from the intrinsic graphene properties as discussed above. On the other hand, the role of defects and edge states as well as the resulting local potential variation deserves further investigations.

Our observed CNP photocurrent and the associated unique kinematics of interacting Dirac fermions indicate several remarkable characteristics of this prototypical two-dimensional Dirac material. First, the carrier relaxation is dominated by electron–electron scattering under our experimental conditions. Since the electron–phonon and electron–impurity scattering processes depend weakly on the Fermi energy (see Supplementary Section 1.2 for discussions), the sharply emergent Dirac-point photocurrent suggests that the contribution from these current-relaxation processes is significantly weaker compared to that of the electron–electron scattering[9,18,21,33]. Second, our results demonstrate that the relaxation of highly nonequilibrium carriers can be strongly affected by the low-energy Dirac cone of graphene, giving rise to observable consequences even in steady-state measurements. Such a remote yet strong coupling between high-energy carriers and low-energy band properties provides a novel approach to probe the low-energy physics of Dirac materials by optical and optoelectronic means. Finally, the CNP photocurrent can inspire much future research. For instance, it is of interest to study the CNP photocurrent by time-resolved near-field measurements. The time-resolution and finer spatial resolution can directly probe the relaxation timescale and ballistic travel distance for the local initial photocurrent $\mathbf{j}_{\mathrm{local}}$. Moreover, by using graphene with a different layer number and stacking order, one can explore how the modified electronic structure affects the CNP photocurrent.

Besides the fundamental significance as mentioned above, our finding of the CNP photocurrent holds promise for applications such as ultrahigh-speed and ultra-broadband optoelectronics. As the CNP photocurrent is carried at the group velocity of unthermalized electrons, it should exhibit an ultrafast response time, possibly leading to ballistic photodetectors. In addition, charge-neutral graphene exhibits strong interband absorption from the visible to far-infrared range, in contrast to conventional doped-graphene devices that suffer from Pauli blockade in the low-energy range. With carefully designed patterning, the CNP graphene devices pave the way for high-speed photodetection and efficient energy harvesting in the full electromagnetic spectrum (see Supplementary Sections 3.3 and 8 for the infrared photocurrent data and a detailed discussion on applications).

Online content

Any methods, additional references, Nature Research reporting summaries, source data, statements of data availability and associated accession codes are available at https://doi.org/10.1038/s41565-018-0323-8.

Received: 29 November 2017; Accepted: 9 November 2018;
Published online: 17 December 2018

References

1. Neto, A. C., Guinea, F., Peres, N., Novoselov, K. S. & Geim, A. K. The electronic properties of graphene. *Rev. Mod. Phys.* **81**, 109–162 (2009).
2. Sarma, S. D., Adam, S., Hwang, E. & Rossi, E. Electronic transport in two-dimensional graphene. *Rev. Mod. Phys.* **83**, 407–470 (2011).
3. Kotov, V. N., Uchoa, B., Pereira, V. M., Guinea, F. & Neto, A. C. Electron–electron interactions in graphene: current status and perspectives. *Rev. Mod. Phys.* **84**, 1067–1126 (2012).
4. Crossno, J. et al. Observation of the Dirac fluid and the breakdown of the Wiedemann–Franz law in graphene. *Science* **351**, 1058–1061 (2016).
5. Bandurin, D. et al. Negative local resistance caused by viscous electron backflow in graphene. *Science* **351**, 1055–1058 (2016).
6. Fritz, L., Schmalian, J., Müller, M. & Sachdev, S. Quantum critical transport in clean graphene. *Phys. Rev. B* **78**, 085416 (2008).
7. Foster, M. S. & Aleiner, I. L. Slow imbalance relaxation and thermoelectric transport in graphene. *Phys. Rev. B* **79**, 085415 (2009).
8. Tomadin, A., Brida, D., Cerullo, G., Ferrari, A. C. & Polini, M. Nonequilibrium dynamics of photoexcited electrons in graphene: collinear scattering, Auger processes, and the impact of screening. *Phys. Rev. B* **88**, 035430 (2013).
9. Brida, D. et al. Ultrafast collinear scattering and carrier multiplication in graphene. *Nat. Commun.* **4**, 1987 (2013).
10. Junck, A., Refael, G. & von Oppen, F. Current amplification and relaxation in Dirac systems. *Phys. Rev. B* **90**, 245110 (2014).
11. Lewandowski, C. & Levitov, L. Photoexcitation cascade and quantum-relativistic jets in graphene. *Phys. Rev. Lett.* **120**, 076601 (2018).
12. Lee, E. J., Balasubramanian, K., Weitz, R. T., Burghard, M. & Kern, K. Contact and edge effects in graphene devices. *Nat. Nanotech.* **3**, 486–490 (2008).
13. Park, J., Ahn, Y. & Ruiz-Vargas, C. Imaging of photocurrent generation and collection in single-layer graphene. *Nano Lett.* **9**, 1742–1746 (2009).
14. Xu, X., Gabor, N. M., Alden, J. S., van der Zande, A. M. & McEuen, P. L. Photo-thermoelectric effect at a graphene interface junction. *Nano Lett.* **10**, 562–566 (2009).
15. Gabor, N. M. et al. Hot carrier-assisted intrinsic photoresponse in graphene. *Science* **334**, 648–652 (2011).
16. Sun, D. et al. Ultrafast hot-carrier-dominated photocurrent in graphene. *Nat. Nanotech.* **7**, 114–118 (2012).
17. Freitag, M., Low, T., Xia, F. & Avouris, P. Photoconductivity of biased graphene. *Nat. Photon.* **7**, 53–59 (2013).
18. Tielrooij, K. et al. Photoexcitation cascade and multiple hot-carrier generation in graphene. *Nat. Phys.* **9**, 248–252 (2013).
19. Graham, M. W., Shi, S.-F., Ralph, D. C., Park, J. & McEuen, P. L. Photocurrent measurements of supercollision cooling in graphene. *Nat. Phys.* **9**, 103–108 (2013).
20. Ma, Q. et al. Competing channels for hot-electron cooling in graphene. *Phys. Rev. Lett.* **112**, 247401 (2014).
21. König-Otto, J. et al. Slow noncollinear Coulomb scattering in the vicinity of the Dirac point in graphene. *Phys. Rev. Lett.* **117**, 087401 (2016).
22. Sun, D. et al. Coherent control of ballistic photocurrents in multilayer epitaxial graphene using quantum interference. *Nano Lett.* **10**, 1293–1296 (2010).
23. Sun, D. et al. Current relaxation due to hot carrier scattering in graphene. *New J. Phys.* **14**, 105012 (2012).
24. Woessner, A. et al. Near-field photocurrent nanoscopy on bare and encapsulated graphene. *Nat. Commun.* **7**, 10783 (2016).
25. Cao, H. et al. Photo-Nernst current in graphene. *Nat. Phys.* **12**, 236–239 (2016).

26. Wu, S. et al. Multiple hot-carrier collection in photo-excited graphene moire superlattices. *Sci. Adv.* **2**, e1600002 (2016).
27. Kim, Y. D. et al. Focused-laser-enabled p–n junctions in graphene field-effect transistors. *ACS Nano* **7**, 5850–5857 (2013).
28. Rao, G., Freitag, M., Chiu, H.-Y., Sundaram, R. S. & Avouris, P. Raman and photocurrent imaging of electrical stress-induced p–n junctions in graphene. *ACS Nano* **5**, 5848–5854 (2011).
29. Song, J. C. & Levitov, L. S. Shockley–Ramo theorem and long-range photocurrent response in gapless materials. *Phys. Rev. B* **90**, 075415 (2014).
30. Van Ostaay, J., Akhmerov, A., Beenakker, C. & Wimmer, M. Dirac boundary condition at the reconstructed zigzag edge of graphene. *Phys. Rev. B* **84**, 195434 (2011).
31. Allen, M. T. et al. Spatially resolved edge currents and guided-wave electronic states in graphene. *Nat. Phys.* **12**, 128–133 (2015).
32. Shalom, M. B. et al. Quantum oscillations of the critical current and high-field superconducting proximity in ballistic graphene. *Nat. Phys.* **12**, 318–322 (2016).
33. Song, J. C., Tielrooij, K. J., Koppens, F. H. & Levitov, L. S. Photoexcited carrier dynamics and impact-excitation cascade in graphene. *Phys. Rev. B* **87**, 155429 (2013).

Acknowledgements

We thank L. Levitov, V. Phong, F. Koppens, K.-J. Tielrooij, M. Lundeberg, A. Woessner and O. Shtanko for discussions. We also thank Y. Sun and B. Han for help with device fabrication. Work in the P.J.-H. group was partly supported by the Center for Excitonics, an Energy Frontier Research Center funded by the US Department of Energy (DOE), Office of Science, Office of Basic Energy Sciences (BES) under award number DESC0001088 (fabrication and measurement) and partly through AFOSR grant number FA9550-16-1-0382 (data analysis), as well as the Gordon and Betty Moore Foundation's EPiQS Initiative through grant number GBMF4541 to P.J.-H. This work made use of the MRSEC Shared Experimental Facilities at MIT, supported by the National Science Foundation (NSF) under award number DMR-14-19807 and of Harvard CNS, supported by NSF ECCS under award number 1541959. Y.C., Y.L., T.P., W.F., J.K., S.-Y.X. and N.G. acknowledge funding support by the STC Center for Integrated Quantum Materials, NSF grant number DMR-1231319. Y.L. and T.P. also acknowledge the US Army Research Office through the MIT Institute for Soldier Nanotechnologies, under award number W911NF-18-2-0048. K.W. and T.T. acknowledge support from the Elemental Strategy Initiative conducted by the MEXT, Japan, JSPS KAKENHI grant numbers JP18K19136 and the CREST (JPMJCR15F3), JST. N.M.G. is supported by the Air Force Office of Scientific Research Young Investigator Program (YIP) award no. FA9550-16-1-0216 and by the NSF Division of Materials Research CAREER award no. 1651247. N.M.G. also acknowledges support through a Cottrell Scholar Award, and through the Canadian Institute for Advanced Research (CIFAR) Azrieli Global Scholar Award. J.C.W.S. acknowledges support from the Singapore National Research Foundation (NRF) under NRF fellowship award NRF-NRFF2016-05 and a Nanyang Technological University (NTU) start-up grant (NTU-SUG).

Author contributions

Q.M. and N.M.G. conceived the experiment. Q.M. and N.L.N. fabricated the devices. Y.L. fabricated additional devices shown in the Supplementary Information under the supervision of T.P. Q.M., T.H.D. and N.M.G. carried out the photocurrent measurements. Q.M., C.H.L. and Y.C. analysed and simulated the data under supervision from P.J.-H. W.F. and J.K. grew the CVD graphene. K.W. and T.T. synthesized the BN crystals. J.C.W.S. and J.F.K. contributed to theoretical discussions. Q.M., C.H.L., J.C.W.S., S.-Y.X., N.G. and P.J.-H. co-wrote the paper with input from all the authors.

Competing interests

The authors declare no competing interests.

Additional information

Supplementary information is available for this paper at https://doi.org/10.1038/s41565-018-0323-8.

Reprints and permissions information is available at www.nature.com/reprints.

Correspondence and requests for materials should be addressed to N.M.G. or P.J.

Publisher's note: Springer Nature remains neutral with regard to jurisdictional claims in published maps and institutional affiliations.

Methods

Device fabrication. We obtained graphene samples by mechanical exfoliation of graphite crystals. The graphene samples for Devices 1–4 were deposited on degenerately doped silicon substrates with a 285 nm oxide epilayer. We patterned graphene into different geometries by e-beam lithography and O_2 plasma etching, and attached 0.8/80-nm Cr/Au electrodes by thermal evaporation. Our devices exhibit low residue doping and no photogating effect. Samples with hBN substrates are presented in Supplementary Section 3.5. The mobility of Devices 1–4 is ~10,000 $cm^2 V^{-1} s^{-1}$.

Scanning photocurrent measurements. We mounted the devices in a Janis ST-500 helium optical cryostat with tunable temperature down to $T = 4$ K. The electrical feed-throughs and the optical windows in the cryostat allow us to measure the source–drain current of the devices under simultaneous laser illumination. We focused the laser (wavelength $\lambda = 850$ nm) onto the samples with a spot diameter of 1 μm by using a 60× microscope objective. The laser spot was scanned over the graphene devices using a two-axis piezoelectrically controlled mirror. We recorded both the direct reflection of the laser and the photocurrent signal as a function of the laser position. Comparison of the reflection image and the photocurrent image allows us to identify the position of the photocurrent signal on the devices.